⌘ *Author's Choice*

THE JOURNAL OF BIOLOGICAL CHEMISTRY VOL. 287, NO. 37, pp. 31349–31358, September 7, 2012
© 2012 by The American Society for Biochemistry and Molecular Biology, Inc. Published in the U.S.A.

Structure and Mechanism of Human UDP-xylose Synthase

EVIDENCE FOR A PROMOTING ROLE OF SUGAR RING DISTORTION IN A THREE-STEP CATALYTIC CONVERSION OF UDP-GLUCURONIC ACID[*][S]

Received for publication, May 30, 2012, and in revised form, July 17, 2012 Published, JBC Papers in Press, July 18, 2012, DOI 10.1074/jbc.M112.386706

Thomas Eixelsberger[‡1], Sabine Sykora[‡1], Sigrid Egger[‡§¶], Michael Brunsteiner[‡‖], Kathryn L. Kavanagh[§], Udo Oppermann[§], Lothar Brecker[‡‡], and Bernd Nidetzky[‡¶‖2]**

From the [‡]Institute of Biotechnology and Biochemical Engineering, Graz University of Technology, A-8010 Graz, Austria, the [§]Structural Genomics Consortium, University of Oxford, Oxford OX3 7DQ, United Kingdom, the [¶]Austrian Centre of Industrial Biotechnology (ACIB), A-8010 Graz, Austria, the [‖]Research Center Pharmaceutical Engineering (RCPE), A-8010 Graz, Austria, the [**]Botnar Research Centre, NIHR Oxford Biomedical Research Unit, University of Oxford, Oxford OX3 7LD, United Kingdom, and the [‡‡]Institute of Organic Chemistry, University of Vienna, A-1090 Vienna, Austria

Background: Human UDP-xylose synthase (hUXS1) is responsible for conversion of UDP-glucuronic acid to UDP-xylose.
Results: Crystal structure, molecular dynamics simulations, and reaction course analysis give conclusive insight into the enzymatic mechanism in three catalytic steps.
Conclusion: Distortion of sugar pyranose ring in bound substrate facilitates enzymatic reaction.
Significance: A detailed mechanism for catalysis by hUXS1 is proposed.

UDP-xylose synthase (UXS) catalyzes decarboxylation of UDP-D-glucuronic acid to UDP-xylose. In mammals, UDP-xylose serves to initiate glycosaminoglycan synthesis on the protein core of extracellular matrix proteoglycans. Lack of UXS activity leads to a defective extracellular matrix, resulting in strong interference with cell signaling pathways. We present comprehensive structural and mechanistic characterization of the human form of UXS. The 1.26-Å crystal structure of the enzyme bound with NAD$^+$ and UDP reveals a homodimeric short-chain dehydrogenase/reductase (SDR), belonging to the NDP-sugar epimerases/dehydratases subclass. We show that enzymatic reaction proceeds in three chemical steps via UDP-4-keto-D-glucuronic acid and UDP-4-keto-pentose intermediates. Molecular dynamics simulations reveal that the D-glucuronyl ring accommodated by UXS features a marked $^4C_1$ *chair* to $B_{O,3}$ *boat* distortion that facilitates catalysis in two different ways. It promotes oxidation at C_4 (step 1) by aligning the enzymatic base Tyr^{147} with the reactive substrate hydroxyl and it brings the carboxylate group at C_5 into an almost fully axial position, ideal for decarboxylation of UDP-4-keto-D-glucuronic acid in the second chemical step. The protonated side chain of Tyr^{147} stabilizes the enolate of decarboxylated C_4 keto species ($^2H_1$ *half-chair*) that is then protonated from the *Si* face at C_5, involving water coordinated by Glu^{120}. Arg^{277}, which is positioned by a salt-link interaction with Glu^{120}, closes up the catalytic site and prevents release of the UDP-4-keto-pentose and NADH intermediates. Hydrogenation of the C_4 keto group by NADH, assisted by Tyr^{147} as catalytic proton donor, yields UDP-xylose adopting the relaxed $^4C_1$ *chair* conformation (step 3).

Proteoglycans are complex assemblies between proteins and linear glycosaminoglycan polysaccharides such as heparan sulfate and chondroitin sulfate (1). They are found in all connective tissues of vertebrates, and on the surfaces of many cell types as components of the extracellular matrix or the glycocalix (1–3). Due to hydration of their glycosaminoglycan chains, proteoglycans impart hydrostatic and elastic properties to the extracellular matrix. As receptors, proteoglycans are critically involved in cell signaling, with consequent effects on tissue development in health or disease (*e.g.* cancer) (1–6). Association between glycosaminoglycan molecules and the protein core of the proteoglycan usually involves enzymatic transfer of a xylosyl residue from UDP-xylose to a protein serine (7). Covalent attachment of the xylosyl group is the first step in generating a functional tetrasaccharide linker on which glycosaminoglycan chain elongation takes place. The UDP-xylose precursor is derived from UDP-glucuronic acid through complex oxidoreductive decarboxylation catalyzed by UDP-xylose synthase (UXS; EC 4.1.1.35; other names: UDP-glucuronic acid decarboxylase; UDP-glucuronic acid carboxylyase) (8, 9). Adequate supply of UDP-xylose was shown in zebrafish to be essential for functional deposition of proteoglycans in the extracellular matrix (10). Defects in production and organization of the extracellular matrix resulting from insufficient UXS[3] activity were correlated with alterations in cell signaling pathways, mirrored in the impaired morphogenesis of various tissues, including the bone. The central and universal biological importance of UXS in vertebrates, including mammals, therefore raises considerable interest in structural and functional properties of

---

[*] This work was supported by the Austrian Science Fund DK Molecular Enzymology Grant W901-B05 and the SGC. The SGC is a registered charity (number 1097737) that receives funds from multiple sources.
⌘ *Author's Choice*—Final version full access.
[S] This article contains supplemental "Methods" and Figs. S1–S5.

[1] Both authors contributed equally to this work.

[2] To whom correspondence should be addressed: Institute of Biotechnology and Biochemical Engineering, Graz University of Technology, Petersgasse 12/I, 8010 Graz, Austria. Tel.: 43-316-873-8400; Fax: 43-316-873-108400; E-mail: bernd.nidetzky@tugraz.at.

[3] The abbreviations used are: UXS, UDP-xylose synthase; UDP-GlcUA, UDP-glucuronic acid; hUXS1, human form of UXS; SeMet, selenomethionine; SDR, short-chain dehydrogenase/reductase; MD, molecular dynamics.

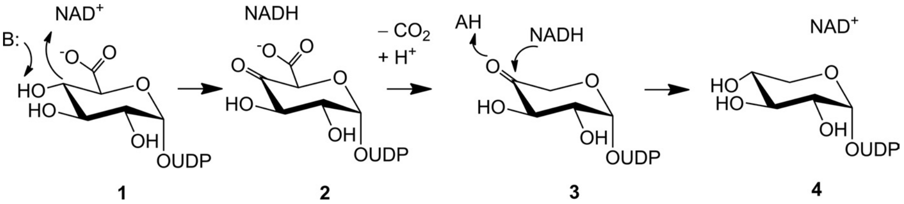

SCHEME 1. **Proposed course of the UXS-catalyzed reaction.** See text for further explanations.

the enzyme. In this work, we present a comprehensive characterization of the human form of UXS (hUXS1) that involved determination of a crystal structure at 1.26-Å resolution.

Phylogenetic analysis reveals that UXS is one of the most strongly conserved nonmitochondrial proteins in nature, with about 57% sequence identity shared between hUXS1 and various bacterial enzyme forms (10). The physiological involvement of UXS differs across the three domains of life, and besides the above described synthesis of protein-linked glycosaminoglycans (7), it also includes the formation of xylose-containing polysaccharides in plants (11) and microorganisms (12–15). Even though UXS activity has been reported in various organisms and cell types, there have only been a few studies of the isolated enzyme. Working with UXS from wheat germ and the fungus *Cryptococcus laurentii*, Feingold and colleagues (16) have developed an ingenious chemical proposal that is shown in Scheme 1. The reaction catalyzed by UXS starts with oxidation of the C_4 alcohol in UDP-glucuronic acid by enzyme-bound NAD^+. The resulting UDP-4-keto-glucuronic acid undergoes decarboxylation, followed by protonation to yield UDP-4-keto-pentose. Keto group reduction by the NADH still bound to the enzyme occurs with retention of the original stereochemistry at C_4, giving UDP-xylose as product. A recent NMR study of a bacterial UXS ortholog appears consistent with the proposed reaction course (17). These insights into the enzymatic transformation notwithstanding, the catalytic mechanism of UXS is fundamentally unknown. The mechanism merits a detailed investigation as it is both biologically very important and chemically intriguing (18–19).

Based on similarity at the primary structure level, hUXS1 is classified in the short-chain dehydrogenase/reductase (SDR) superfamily of proteins (20). hUXS1 is most closely related to the divergent group of so-called "extended SDRs" that include nucleotide-sugar epimerization and dehydration as their main activities (for reviews on enzyme mechanisms, see Refs. 18, 19, 21, and 22). Sequence alignment (supplemental Fig. S1) suggests that hUXS1 is equipped with the canonical SDR active site in which a highly conserved triad of residues (Thr^{118}, Tyr^{147}, Lys^{151}) is probably involved in catalytic oxidoreduction. However, there are also variable features (*e.g.* Glu^{120}, Arg^{277}) that could have a decisive role in the enzymatic conversion. Herein we report on results of structure determination, molecular dynamics (MD) simulation, and reaction course analysis for wild-type and mutated forms of hUXS1, which in combination give conclusive evidence on the enzyme mechanism, delineating how individual active site residues assist the reaction in each of its three catalytic steps. A significant feature of the mechanism is that the catalytic reaction course is underpinned by promoting conformational changes in the pyranose ring structure of the UDP-sugar substrate/intermediate. We have identified the protein residues responsible for the sugar ring distortion and clarified their role in catalysis.

EXPERIMENTAL PROCEDURES

Materials—Unless stated otherwise, all materials were of highest purity available from Roth (Karlsruhe, Germany). UDP-glucuronic acid (>98% purity) was obtained from Sigma and UDP-xylose (>95% purity) from Carbosynth (Compton, UK). D_2O (99.8% D) was purchased from ARMAR Chemicals (Döttingen, Switzerland).

Protein Preparation—We used a truncated form of hUXS1 (residues 85–402) that was optimized for crystallization. The construct was designed to encompass the entire Rossmann-fold and ordered regions at the C terminus. Regions predicted to encode a signal peptide and transmembrane helix were deleted from the N terminus, whereas a predicted random coil was deleted from the C terminus. The final construct contained a 23-amino acid long N-terminal peptide comprising the His_6 tag. We refer to this construct throughout when hUXS1 is mentioned. Experimental procedures used for recombinant protein preparation are described in full detail in the supplemental "Methods". Briefly, the enzyme was overexpressed in *Escherichia coli* Rosetta 2(DE3) using the pET-derived expression vector p11 (wild-type) or the pNIC28-Bsa4 plasmid (mutants). After high-pressure cell disruption (1500 psi), the enzyme was isolated from the crude extract using a Cu^{2+}-loaded IMAC-Sepharose High Performance column (GE Healthcare). Stepwise elution with imidazole was employed to yield highly pure hUXS1 (checked by SDS-PAGE). Imidazole was removed by buffer exchange to 50 mM Tris/HCl (pH 7.5) containing 5% glycerol and 1 mM DTT using a NAP-25 desalting column (GE Healthcare) or Vivaspin-20 centrifugal concentrator (Sartorius Stedim, Göttingen, Germany). Preparations of hUXS1 were stored at −70 °C. For crystallization experiments, SeMet-labeled enzyme was produced in *E. coli* B834(DE3) grown on SelenoMethionine Medium Base plus Nutrient Mix containing SeMet at 40 mg/liter (Molecular Dimensions, Newmarket, UK). Site-directed mutagenesis was performed using standard protocols. Mutants purified similarly as the wild-type enzyme.

Crystallization, Data Collection, and Refinement—SeMet-labeled hUXS1 containing 5 mM NAD^+ and 5 mM UDP was concentrated to 12 mg/ml (~0.3 mM). Crystals were obtained by vapor diffusion at 20 °C in 150-nl sitting drops, equilibrated against mother liquor containing 20% PEG 6000, 10% ethylene glycol, and 0.2 M NaCl in 0.1 M HEPES (pH 7). Diffraction data to 1.2 Å were collected at 100 K at the Swiss Light Source station X10SA using a MARMOSAIC 225 mm CCD detector at a single wavelength near the selenium absorption edge ($\lambda = 0.9795$ Å).

Data were indexed and integrated in MOSFLM (23) and scaled in SCALA (23). Merging of the data and analysis of systematic absences identified the space group as P121, with the following cell dimensions: $a = 46$ Å, $b = 45$ Å, $c = 85$ Å; $\alpha = 90°$, $\beta = 97°$, $\gamma = 90°$. The program SHELXD (24) located 11 SeMet residues in hUXS1, indicating complete labeling of the protein. SHELXE was used for phasing and automated chain tracing was done with ARP/wARP. The hUXS1 structure was manually rebuilt in COOT (25), and restrained refinement was performed using REFMAC5 (26). When electron density showed the presence of NAD^+ and UDP in the active site as well as an additional UDP forming a crystal contact, the ligands were fitted to the density and included in the refinement. Although the full range of data to 1.2 Å was used in refinement, analysis of data completeness and signal to noise suggests that 1.26 Å is a more reasonable estimate of the resolution of the model. Data collection and refinement statistics are summarized in Table 1.

Molecular Dynamics Simulation—All MD simulations were performed using Gromacs (27). For the protein and water a variation of the Amber99sb (28) and the TIP3P (29) force fields was used. For NAD, substrate, intermediates, and product General Amber Force Field (GAFF) parameters (30) and Gromacs input files were generated using the Amber Antechamber suite of programs (31) together with the perl script amb2gmx (32). As starting structure for MD simulations the crystal structure of UXS (PDB code 2B69) was used, approximate pK_a values of ionizable residues were established using PROPKA (33), and ionizable residues were protonated accordingly. For the MD simulations the protein with substrate, product, or intermediates was positioned in the center of a cubic box with 6.7-nm side length and solvated in ~8,000 water molecules. The appropriate number of water molecules was replaced by sodium ions to neutralize the system. A leapfrog algorithm with a time step of 2 fs was used for integrating the equations of motion. The temperature was kept constant at 300 K using a Nosé-Hoover thermostat (34). Electrostatic long range interactions were accounted for using a particle mesh Ewald algorithm (35). A cut-off of 10 Å was used for the real space part of the Ewald summation and the van der Waals interactions. A constant pressure of 1 atm was maintained using a Berendsen thermostat (36). All bonds including hydrogens were constrained using a LINCS algorithm (37). Conformations were saved every 2 ps. The MD simulations covered a time between 4 and 6 ns. In each case the trajectories covering the last 2 ns were used to calculate hydrogen bonding and average structures. For visual inspection of trajectories and conformations Chimera was used. The trajectories were analyzed with various Gromacs tools and in-house scripts.

Analysis of the Enzymatic Reaction Course—Reactions were performed at 25 °C in 50 mM Tris/HCl buffer (pH 7.5). Substrate and enzyme concentrations as well as reaction times differed depending on the specific experimental setup and are therefore mentioned individually. Reactions were stopped by addition of acetonitrile in a 1:1 volume ratio to buffer. Precipitated protein was removed by centrifugation (10 min, 4 °C, 16,000 × *g*). Samples were analyzed with a reversed phase HPLC (see supplemental "Methods"). It was shown that consumption of UDP-GlcUA proceeded linearly in dependence of reaction time, so that measurements were suitable for calculation of initial rates. Data for kinetic analysis were obtained under conditions in which the concentration of NAD^+ or UDP-GlcUA was varied, whereas the concentration of the respective other substrate was constant (wild-type, 0.5 mM NAD^+ and 2 mM UDP-GlcUA; mutants, 10 mM NAD^+ and 10 mM UDP-GlcUA). V_{max} values were derived from nonlinear fits of the Michaelis-Menten equation. The molarity of enzyme active sites (E) was calculated from the protein concentration, assuming a molecular mass of 38,595 Da for the protein subunit. It was used to determine the turnover number, using the relationship $k_{cat} = V_{max}/E$. Experiments were performed in triplicate (S.D. ≤ 15%).

Transient Kinetic Studies—Experiments were performed at 25 °C with an Applied Photophysics (Leatherhead, UK) model SX.18 MV Stopped-flow Spectrometer. Enzyme was used in a limiting concentration (≤25 μM). A 50 mM Tris/HCl buffer (pH 7.5) was used. Enzyme solution was mixed in 1:1 ratio with substrate solution, yielding concentrations of 0.5 mM NAD^+ and 10 mM UDP-GlcUA, unless stated otherwise. The absorbance of enzyme-bound NADH was measured at 340 nm and converted to concentration using an extinction coefficient of 6,220 M^{-1} cm^{-1}. The stopped-flow instrument had a dead-time of 1.5 ms, and data were recorded up to 1,000 s. Slow reactions catalyzed by hUXS1 mutants were followed additionally in a conventional UV/visible spectrophotometer (Beckman Coulter DU 800), measuring the change in absorbance at 340 nm.

Solvent Kinetic Isotope Effect—For examination of the solvent kinetic isotope effect, a 20 mM potassium phosphate buffer (pH/pD 7.5) in H_2O or D_2O was prepared. The pD was determined as pH meter reading plus 0.4 (38). Concentrations of 10 mM UDP-GlcUA, 0.5 (wild type) or 1 (E120A) mM NAD^+, and 15 (wild type) or 36 (E120A) μM enzyme were used. Enzymes were gel-filtered three times employing deuterated phosphate buffer and equilibrated with solvent prior to the experiments in D_2O. Reactions were stopped after 8 min (wild-type) or 50 min (E120A) by addition of acetonitrile in 1:1 ratio and samples were analyzed on the HPLC. Solvent isotope effects were calculated from the ratio of k_{cat} values measured in H_2O and D_2O.

In Situ NMR Analysis—Enzymatic reactions were performed directly in a 5-mm high precision NMR sample tube (Promochem, Wesel, Germany) and monitored *in situ* over 12 h in the magnet, by recording up to 64 ^1H NMR spectra in regular intervals. For further measurements, samples were kept in a temperature-controlled water bath (30 °C) and measured in unsteady intervals over ~48 h. All spectra were obtained with a Bruker DRX-600 AVANCE spectrometer (Bruker, Rheinstetten, Germany) at 600.13 MHz (^1H) using the Bruker Topspin 1.3 software. Chemical shifts were referenced to external acetone (δH 2.225 ppm). Further details are provided under supplemental "Methods".

Other Methods—Force field tests, nondenaturing anionic PAGE, and HPLC analysis are described in supplemental "Methods" and Fig. S5.

RESULTS AND DISCUSSION

High-resolution Crystal Structure of hUXS1—We solved the crystal structure of hUXS1 in complex with NAD^+ and UDP to

TABLE 1

Crystallographic data collection and refinement statistics

Enzyme complex	hUXS1-UDP-NAD$^+$
PDB accession code	2B69
Synchrotron beamline	SLS, X10SA
Wavelength (Å)	0.9795
Space group	P121
Unit cell dimensions	$a = 46$, $b = 45$, $c = 85$ Å $\alpha = \gamma = 90.0°$ $\beta = 97°$
Resolution range^a (Å)	42–1.20 (1.26–1.20)
No. unique reflections^a	93023 (8576)
Completeness^a (%)	91.3 (58.1)
Mean I/sdI $\langle I/\sigma(I)\rangle^a$	25.2 (1.3)
$R_{\text{merge}}{}^a$ (%)	6.5 (53.7)
Redundancy^a	2.1 (1.3)
Refinement	
No. atoms P/L/O^b	2439/94/353
$R_{\text{work}}/R_{\text{free}}$ (%)	13.4/16.2
R.m.s. deviation bond length^c (Å)	0.014
R.m.s. deviation bond angle (°)	1.506
B_{mean} P/L/O^b (Å^2)	14/28/32

[a] Values in parentheses correspond to data in highest resolution shell.

[b] P/L/O refer to protein, ligand, and solvent atoms.

[c] R.m.s. deviation is root mean square deviation.

a resolution of 1.26 Å (PDB code 2B69; Table 1). The experimental structure consists of a single polypeptide chain of 312 amino acids and is composed of 12 α-helices (37%) and 17 β-strands (Fig. 1*A*, supplemental Fig. S1).[4] The N-terminal His tag in addition to 3 N-terminal residues and 5 C-terminal residues were not visible in electron density maps and were not modeled. Although the asymmetric unit contains a single hUXS1 subunit, analysis of the crystal packing by the program PISA (39) suggests the protein is dimeric. Similar to other dimeric SDRs, the dimer interface is composed of helices $\alpha 5$ and $\alpha 7$, forming a helical bundle as shown in Fig. 1*A*. The monomeric form of hUXS1 has a predicted molecular mass of 38.6 kDa, which was confirmed by SDS-PAGE (supplemental Fig. S2*A*). In nondenaturing anionic PAGE, the enzyme showed a migration behavior consistent with its presence as a homodimer (supplemental Fig. S2*B*). Furthermore, we used gel filtration to estimate an apparent molecular mass of about 70–75 kDa for hUXS1 in solution (data not shown). The structural and biochemical data therefore support the notion that the enzyme is a functional homodimer (calculated mass 77.2 kDa). Mutants of hUXS1 migrated similarly in nondenaturing PAGE, giving evidence that they are also present as dimers in solution (data not shown).

Functionally, hUXS1 can be split into two domains: a large NAD$^+$-binding domain (residues 4–181, 216–242, and 279–294) and a considerably smaller UDP-GlcUA binding domain (residues 182–215, 243–278, and 295–315). The large domain of hUXS1 is built of a seven-stranded parallel β-sheet sandwiched between two arrays of parallel helices with a small helix capping one end of the sheet, resulting in a modified version of the classic Rossmann fold. The UDP-GlcUA binding domain is composed of two small 2-stranded β-sheets (one parallel and one anti-parallel) and a 3-helix bundle. The active site of the enzyme is located in a cavity formed between the two domains (Fig. 1*B*). Fig. 1 shows how NAD$^+$ (*panel C*) and UDP (*panel D*) are accommodated in their respective binding sites on the enzyme. The NAD$^+$ is buried deeply in the protein structure, suggesting that coenzyme is bound tightly by the enzyme. This is consistent with biochemical data indicating that hUXS1 displays about 60% of its maximum activity under assay conditions where no external NAD$^+$ is added (supplemental Fig. S2*C*).

The Active Site of hUXS1—There are 6 highly conserved residues that make up the active site of hUXS1, as shown in Fig. 2. Thr^{118}, Tyr^{147}, and Lys^{151} form the characteristic signature of a typical SDR catalytic center. Ser^{119}, Glu^{120}, and Arg^{277} are distinct features of the UXS group of enzymes (Fig. 1*B*, supplemental Fig. S1). We analyzed binding of the substrate by carrying out an energy-minimized docking of UDP-GlcUA followed by MD simulation of the resulting ternary hUXS1·NAD$^+$·substrate complex. The protein-ligand structure readily converged into a stable conformation that was characterized by a root mean square deviation of ≤ 0.15 nm as compared with the experimental structure (supplemental Fig. S3*A*). Fig. 2 shows that in the modeled structure the D-glucuronyl pyranose ring of UDP-GlcUA was distorted from the expected low-energy $^4C_1$ *chair* conformation to $B_{O,3}$ *boat*. Sugar ring distortion is required for Tyr^{147} to become hydrogen bonded with the C_4 hydroxyl, thus positioning the reactive substrate group for general base catalysis by the tyrosine. The C_4 hydrogen was within plausible reaction distance (3.6 Å) to the NAD$^+$ nicotinamide C_4, suggesting that the modeled complex would be catalytically competent. Hydride transfer would therefore take place with pro-*S* stereospecificity, fully consistent with expectations for a member of the SDR superfamily. Our model further suggests that Thr^{118} contributes to the sugar ring distortion by forming a strong hydrogen bond with the carboxylate group at C_5. In the experimental structure of hUXS1 bound with UDP, Thr^{118} is bonded to a water molecule (Fig. 1*C*). Tyr^{147} and Lys^{151} were hydrogen bonded to the hydroxyls at C_2 and C_3 of the nicotinamide ribose (Fig. 1*C*), respectively, thus facilitating precise relative positioning of reactive parts of substrate and coenzyme at the enzyme active site, as also seen in classical SDR enzymes (40).

Fig. 2 also shows that Ser^{119} is strongly hydrogen bonded with the substrate carboxylate group. The interaction between Glu^{120} and Arg^{277} fastens together two long loops (residues 119–144 and 268–277), thus closing up the active site (Fig. 2, supplemental Fig. S4, *C* and *D*). This loop closing is conducive to catalysis because it brings both Thr^{118} and Ser^{119} into their reactive positions. In the closed conformation of hUXS1, the glucuronyl moiety of the substrate is buried deeply inside the protein structure, whereas the UDP portion is partially solvent exposed (Fig. 1*B*, supplemental Fig. S4, *A* and *B*).

One of the closest structural neighbors of hUXS1 is the decarboxylase domain of ArnA, a bifunctional enzyme from *E. coli* that catalyzes conversion of UDP-GlcUA into UDP-4-amino-4-deoxy-L-arabinose (41–43) (supplemental Fig. S4*E*). Reactions of hUXS1 and ArnA probably proceed on identical paths up to the UDP-4-keto-pentose intermediate, with the exception that ArnA releases the NADH produced. The transformylase domain of ArnA then utilizes UDP-4-keto-pentose in a stereospecific transaminase reaction to give UDP-4-amino-4-deoxy-L-arabinose as the product. A structure of a nonpro-

---

[4] Amino acid numbering for hUXS1 within the manuscript corresponds to PDB structure 2B69. There is an offset of −85 compared with the gene-derived sequence.

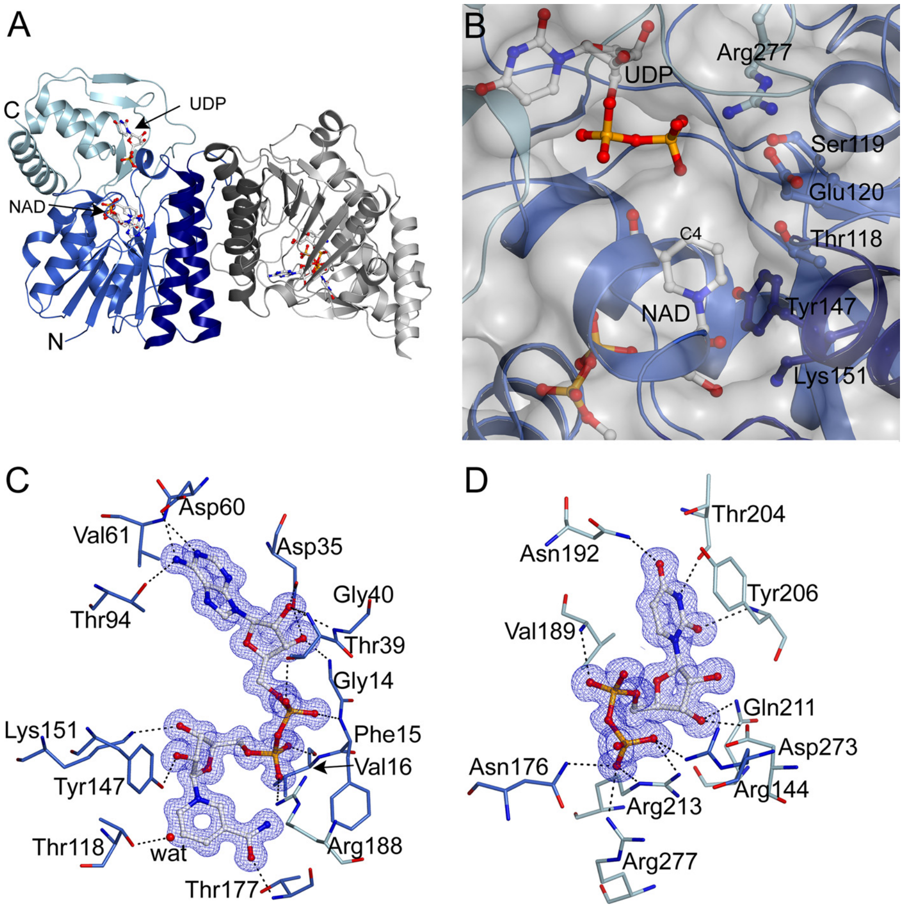

FIGURE 1. **X-ray structure of hUXS1 bound with NAD$^+$ and UDP.** *A*, α-carbon trace of the hUXS1 crystallographic dimer. The single molecule in the asymmetric unit is colored *blue* with the UDP-GlcUA binding domain shown *lighter blue* and the helices at the dimeric interface *darker blue*. A symmetry-related molecule is shown in *gray*. *B*, surface representation of the hUXS1 active site. The NAD$^+$ is buried with C_4 14 Å from the surface at the interface between the two domains. Conserved residues are labeled. *C* and *D*, electron density ($2F_o - F_c$ contoured at 1σ) and hydrogen-bonding interactions $\leq$3.2 Å for bound ligands NAD$^+$ (*C*) and UDP (*D*). A water molecule coordinated to Thr^{118} is shown as a *red sphere*.

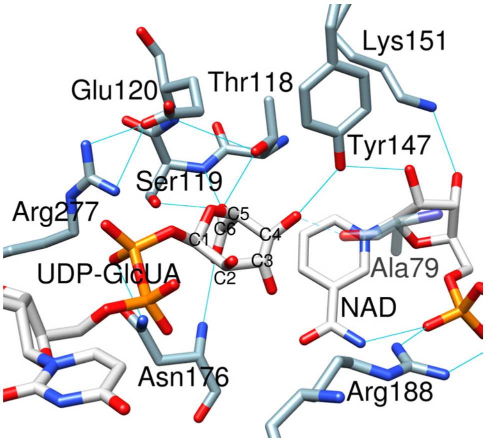

FIGURE 2. **Active site of hUXS1 with the D-glucuronyl ring of UDP-GlcUA accommodated in a distorted $B_{O,3}$ conformation.** Substrate binding mode was obtained by MD simulation. Hydrogen bonds are indicated by *blue lines*. The interaction between Ala^{79} and sugar C_4 oxygen only occurred in <60% of structures during simulation (supplemental Fig. S3*B*) and is therefore shown transparently.

ductive ternary complex of full-length ArnA that has UDP-GlcUA and ATP (as NAD$^+$ surrogate) bound to the decarboxylase domain was solved at 3.0-Å resolution (PDB code 1Z7E). The active sites of hUXS1 and the ArnA decarboxylase domain are similar and the binding sites for substrate and coenzyme appear to be also largely conserved. Interestingly, therefore, the D-glucuronyl ring of substrate bound to ArnA was in the undistorted $^4C_1$ *chair* conformation (42) (supplemental Fig. S4*F*). This may be due to the lack of a reactive nicotinamide moiety on ATP (compared with NAD$^+$), preventing the sugar ring distortion from taking place. In ArnA, Thr^{432} formed a hydrogen bond with the hydroxyl at C_4, whereas Tyr^{463} adopted a position about 5 Å away from the reactive site of the substrate, inconsistent with a direct participation of the tyrosine in catalysis (see later). Our docking experiments reveal that it is possible to accommodate UDP-GlcUA in an "ArnA-like binding mode" in hUXS1. However, under molecular dynamics conditions the enzyme complex structure relaxed immediately to the time-averaged conformation depicted in Fig. 2. Mutagenesis experiments described below strongly support the $B_{O,3}$ *boat* model, which therefore constitutes a highly probable representation of the productive hUXS1 ternary complex.

Reaction Course for Wild-type and Mutated Forms of hUXS1— The course of conversion of UDP-GlcUA by wild-type hUXS1 was recorded using HPLC and *in situ* proton NMR (Fig. 3). The absorbance of NADH was also measured, serving as an on-enzyme spectroscopic probe of the reaction at steady state and under conditions of rapid mixing in a stopped-flow analyzer. Table 2 summarizes the results. UDP-xylose was the sole product of the enzymatic reaction. Traces of UDP-4-keto-pentose were detectable by NMR. Because NADH was also formed in roughly corresponding amounts ($\leq$0.001-fold the molar equivalent of substrate converted) and the relevant NMR signals were relatively broad, it is probable that the enzyme-bound form of the UDP-4-keto-pentose intermediate was observed. Looking at the time domain from milliseconds to about 10 s, in which according to its k_{cat} value the wild-type enzyme would have undergone one full turnover, there was no accumulation of NADH above the steady-state level (Fig. 4*A*). These results immediately imply that in native hUXS1 the decarboxylation of UDP-4-keto-GlcUA and the reduction of UDP-4-keto-pentose are both substantially faster than the initial oxidation of UDP-GlcUA, which is therefore identified as the rate-determining chemistry in the overall reaction. The NMR data also reveal that during reaction in D_2O, the UDP-xylose became deuterium-labeled at the C_5 and the incorporation was stereospecific. The relative small $^3J_{H\text{-}H}$ coupling constant (~5.7 Hz) between the remaining proton at C_5 and the proton at C_4 of the pyranose ring indicate the chiral center at C_5 to be in *S*-configuration and suggest that the deuterium was most probably incorporated at the axial position (Fig. 3, *traces A* and *B*).

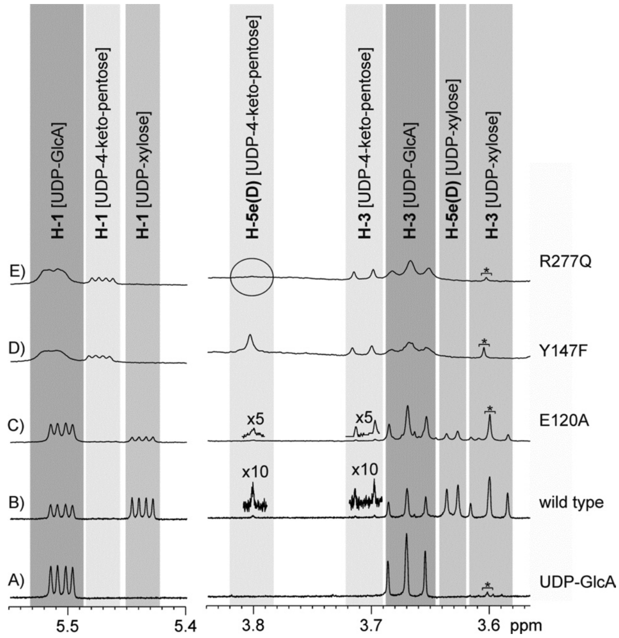

FIGURE 3. **Results from *in situ* NMR experiments with hUXS1.** *Trace A* shows some signals of the substrate UDP-GlcUA at the beginning of the transformations. In *trace B*, additional signals of the final product UDP-xylose are visible. This product is formed during the wild-type catalyzed reaction and contains one deuterium atom in position H-5_{ax}. A further tiny amount of the UDP-4-keto-pentose is detectable, which also carries a deuterium atom in position H-5_{ax}. Transformations catalyzed by the E120A mutant lead to comparable results, as shown in *trace C*. Here also mainly UDP-xylose is accumulated, whereas UDP-4-keto-pentose is undetectable or present only in very tiny concentrations, respectively. Transformations catalyzed by the Y147F mutant exclusively accumulate the intermediate UDP-4-keto-pentose with one deuterium atom in position H-5_{ax} (*trace D*). Transformations with the R277Q mutant (*trace E*) also lead to the same intermediate, which, however, is deuterated twice in position 5. In none of the transformations have any hints for accumulation of the UDP-4-keto-GlcUA been detected. An impurity (TRIS) causes the additional singlet at 3.605 ppm, which is indicated with an *asterisk*.

Fig. 2 suggests that Glu^{120}, Tyr^{147}, and Arg^{277} could be catalytically important, and we examined their roles through characterization of E120A, Y147F, and R277Q mutants. All mutants were less active in terms of k_{cat} than the wild-type enzyme (Table 2). Y147F had completely lost the ability to form UDP-xylose as a product of UDP-GlcUA conversion; R277Q produced only traces of UDP-xylose. Therefore, these two mutants accumulated NADH in amounts corresponding to the molar equivalent of UDP-GlcUA used (Table 2). Reactions of the Y147F and R277Q mutants became stalled at the level of UDP-4-keto-pentose. The product made by Y147F in D_2O contained a single deuterium at C_5, whereas the corresponding product of the reaction of R277Q was doubly deuterated at this position (Table 2 and Fig. 3, *traces D* and *E*). NMR data show that deuterium incorporation by Y147F occurred with the same stereoselectivity as in the wild-type enzyme.

We determined that there was no spontaneous H/D exchange at the C_5 of UDP-GlcUA, UDP-xylose, and UDP-4-keto-pentose in the time span of our experiments. Therefore, a double incorporation of deuterium label into the UDP-4-keto-pentose product necessitates that in the course of the reaction catalyzed by R277Q, the proton initially present at C_5 must have become sufficiently acidic to undergo complete exchange with bulk solvent. Based on chemical considerations, the C_5 proton of UDP-4-keto-GlcUA would be a strong candidate. Consider-

TABLE 2
Kinetic characterization of wild-type and mutated forms of hUXS1

Enzyme	k_{cat}/limiting reaction[a]	K_m UDP-GlcUA	Reaction product[b]	NADH formation[c]	Deuterium incorporation in product at C_5[d]
	s^{-1}	mM			
Wild-type	0.2/oxidation[e]	5.1	**4**, traces of **3**	$\leq$0.001	Axial[f]
E120A	1.7×10^{-3}/reduction[e]	0.7	**4**, traces of **3**[g] (**3** and **4**)	~0.05[g] (~0.5)	Axial[f]
Y147F	1.3×10^{-4}/NA	>30[h]	**3**	~1	Axial[i]
R277Q	1.5×10^{-4}/NA	0.1	**3**, traces of **4**	~1	Double deuteration

[a] Determined from the rate of conversion of UDP-GlcUA.

[b] Notation: **3**, UDP-4-keto-pentose; **4**, UDP-xylose.

[c] Molar ratio of NADH formed and UDP-GlcUA converted; data have S.D. of about 15%.

[d] Determined by ^1H NMR.

[e] Determined by comparing the rate of NADH formation under conditions of rapid mixing in a stopped-flow apparatus to the steady-state rate of formation of UDP-xylose. Note that *reduction* is meant here to involve all reaction steps after formation of UDP-4-keto-GlcUA (**2**), including the decarboxylation. NA, not applicable.

[f] Stereochemical assignment is made for **4**. It follows from the proposed enzymatic reaction that **3** will have deuterium incorporated at C_5 with the same stereochemistry as **4**.

[g] The molar ratio of **4** and **3** decreased in response to increase of UDP-GlcUA (**1**) concentration, from the shown value at 10 mM of **1** to the value in parentheses at 50 mM of **1**.

[h] No exact determination possible, as no substrate saturation could be reached.

[i] Inferred from equivalence of ^1H spectra of **3** formed by Y147F mutant and wild-type enzyme.

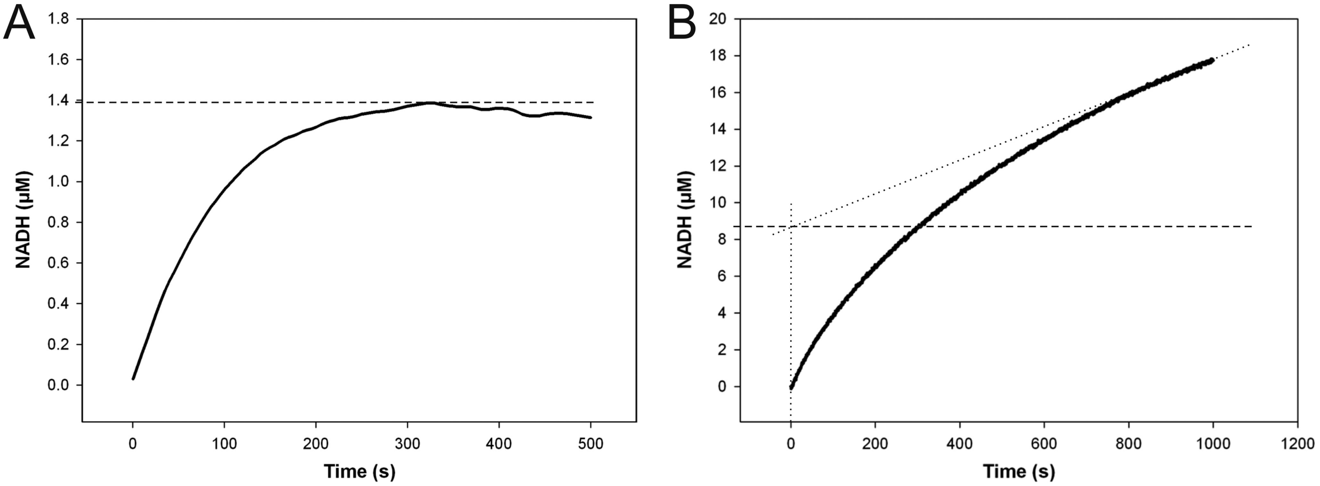

FIGURE 4. **Stopped-flow progress curves of NADH formation in reactions catalyzed by wild-type hUXS1 (*A*) and E120A mutant (*B*).** Reactions were performed using 0.5 mM NAD^+ and 10 mM UDP-GlcUA. *A,* reaction with 25 μM wild-type enzyme. There was no accumulation of NADH above 0.055 mol enzyme equivalents (1.4 μM; *dashed line*). *B,* the E120A mutant (15 μM) accumulated up to 0.58 mol enzyme equivalents (8.7 μM; *dashed line*) of NADH in the pre-steady state, indicating a shift in the rate-determining step from NADH formation to NADH consumption.

ing that the R277Q mutant did not produce UDP-4-keto-GlcUA in detectable amounts (Fig. 3), we conclude that the H/D exchange must have taken place at the active site of the mutant. Occurrence of this exchange was not primarily determined by intermediate lifetime, as we could show that the formation of NADH did not proceed ahead of production of UDP-4-keto-pentose during the first turnover. This would be the case if decarboxylation of UDP-4-keto-GlcUA had become the slowest step of the overall reaction of the mutant. Enhanced readiness of R277Q-bound UDP-4-keto-GlcUA to undergo H/D exchange must therefore be ascribed to a direct effect of the mutation on the solvent accessibility of the intermediate, reinforced by results of MD simulations to be described below.

Product distribution of the E120A-catalyzed reaction was dependent on the UDP-GlcUA concentration used, whereupon UDP-4-keto-pentose formation was promoted at high substrate levels. Unlike wild-type enzyme, E120A accumulated substantial amounts of NADH (up to 0.58 molar enzyme equivalents) in the pre-steady state of their reactions (Fig. 4*B*). Therefore, rate limitation was shifted from NADH formation (substrate oxidation) in wild-type enzyme to NADH consumption (substrate reduction including decarboxylation) in the mutant. Interestingly, the k_{cat} for E120A displayed a solvent kinetic isotope effect of 4.4 ($= k_{cat}(H_2O)/k_{cat}(D_2O)$), whereas that of wild-type enzyme was just 1.4.[5]

Sugar Ring Distortions at the Active Site and Their Role in Promoting Catalysis—Fig. 2 suggests that substrate binding involves considerable strain on the D-glucuronyl pyranose ring. We therefore performed MD simulations on all complexes of the proposed enzymatic reaction (Scheme 1). Results indicate a trajectory of the pyranose ring pucker that moves from the relaxed $^4C_1$ *chair* in free substrate via $B_{O,3}$ *boat* in Michaelis complex (Fig. 5*A*) to a ^2S_O *skew-boat* conformation in the UDP-4-keto-GlcUA intermediate (Fig. 5*B*). This trajectory, which is plausible as it contains only conformations accessible to the D-glucuronyl ring in solution (44, 45), appears to be highly conducive to UXS catalysis in each step. The $^4C_1 \rightarrow B_{O,3}$ transition serves to align the catalytic groups for NAD^+-dependent oxidation at C_4, however, already in expectation of the subsequent decarboxylation because the carboxylate group at C_5 is brought into an axial position that makes it an excellent leaving group. The $B_{O,3} \rightarrow {}^2S_O$ transition, which accompanies substrate oxidation, additionally involves a slight tilt of the pyranose ring at the active site (*cf.* Fig. 5, *A* and *B*), resulting in distinctly altered hydrogen bonding of the 4-keto-GlcUA moiety with the enzyme as compared with substrate. In particular, contact between Thr^{118} and the carboxylate group is disrupted and the threonine now interacts with the 4-keto group of the intermediate. This new arrangement of hydrogen bonds (involving Thr^{118} and Ser^{119}) would provide excellent stabilization for β-keto acid decarboxylation (46). Generating the E120A mutant *in silico*, we find that due to loss of hydrogen bonding capability in the mutant as compared with wild-type enzyme, substrate distortion in the Michaelis complex is decreased substantially and equatorial-to-axial reorientation of the carboxylate group of the substrate does not occur (Fig. 5*E*). Therefore, these findings could explain the dual effect of the $Glu^{120} \rightarrow$ Ala substitution that reaction is slowed already at the substrate oxidation step, whereas at the same time rate limitation is shifted to the following steps of the catalytic cycle.

MD simulation of the substrate complex of the R277Q mutant revealed an even larger pyranoside ring distortion than in wild-type enzyme, involving a different way of accommodating the carboxylate at C_5 in which Thr^{118} has no role (Fig. 5*F*). Reactive carbons on substrate and NAD^+ appear to be better aligned for hydride transfer in the wild-type complex as compared with the R277Q complex, providing a tentative explanation for the low reactivity of the mutant in the initial oxidation step of the catalytic reaction. The modeled UDP-4-keto-GlcUA complex of R277Q (Fig. 5*G*) differs from the corresponding wild-type complex (Fig. 5*B*) in that the pyranose ring of the 4-keto-GlcUA moiety adopts a $^1C_4$ (rather than ^2S_O) conforma-

---

[5] Reaction conditions were used where E120A mutant forms UDP-xylose and only trace amounts of UDP-4-keto-pentose upon conversion of UDP-GlcUA.

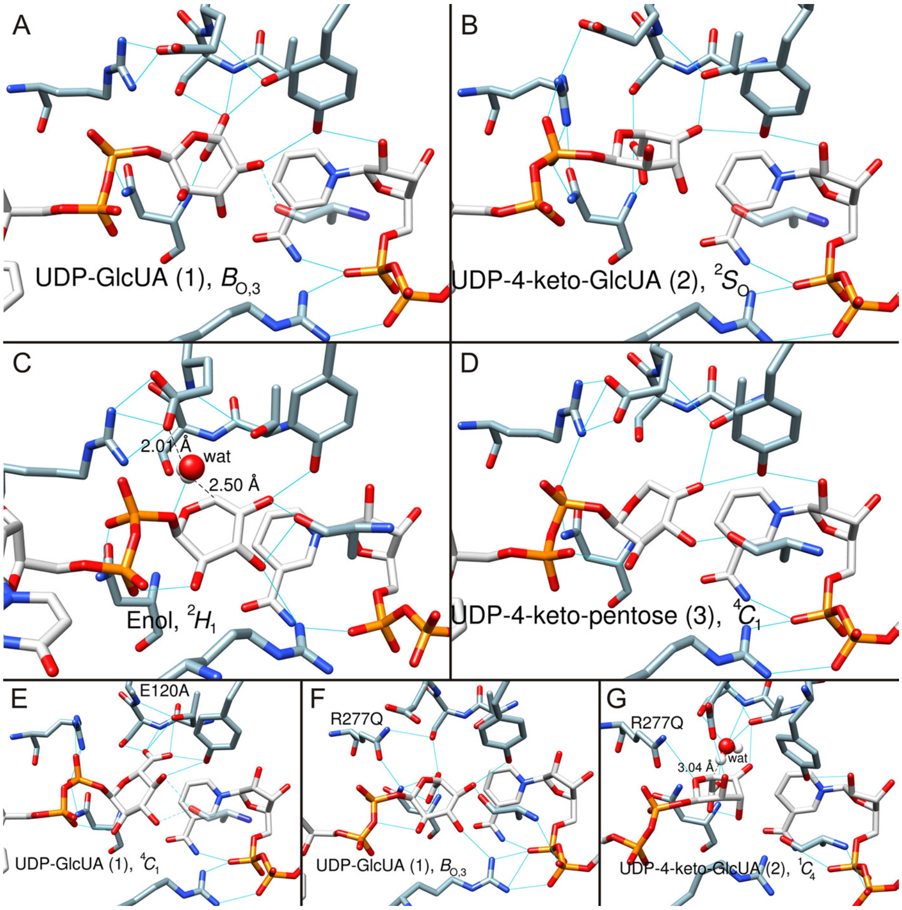

FIGURE 5. **Trajectory of sugar ring conformation along the hUXS1 reaction coordinate determined by MD simulation.** Numbering of substrate/intermediate corresponds to the designation shown in Schemes 1 and 2. *Blue lines* indicate hydrogen bonds. Amino acid residues (except mutations) are not labeled here for better clarity (refer to Fig. 2). *A,* substrate UDP-GlcUA, **1**, is in $B_{O,3}$ *boat* conformation. *B,* UDP-4-keto-GlcUA intermediate, **2**, in ^2S_O *skew-boat* conformation. *C,* UDP-4-keto-pentose, enol form, in $^2H_1$ *half-chair* conformation. The water that protonates C_5 is shown in *white/red*. *D,* UDP-4-keto-pentose intermediate, **3**, in $^4C_1$ *chair* conformation. *E,* mutant complex E120A·NAD$^+$·UDP-GlcUA. The substrate, **1**, is in the $^4C_1$ *chair* conformation. *F,* mutant complex R277Q·NAD$^+$·UDP-GlcUA. The substrate, **1**, is in the $B_{O,3}$ *boat* conformation. *G,* mutant complex R277Q·NADH·UDP-4-keto-GlcUA. The 4-keto-D-glucuronyl ring of UDP-4-keto-GlcUA, **2**, is in a $^1C_4$ *chair* conformation. MD simulation revealed a water molecule possibly involved in hydrogen/deuterium exchange at C_5 of UDP-4-keto-GlcUA in the R277Q mutant. The water is shown in *white/red*. Note that the modeled structure of the corresponding NADH·UDP-4-keto-GlcUA complex of the wild-type enzyme (*panel B*) lacked water in a position suitable for hydrogen/deuterium exchange, consistent with only a single deuterium being incorporated during reaction in D_2O.

tion. However, the carboxylate group of the substrate is still oriented axial, consistent with experimental observation that R277Q forms decarboxylated product exclusively. Interestingly, the mutant complex shows a water molecule in the immediate proximity to the C_5 proton of UDP-4-keto-GlcUA, suggesting how H/D exchange could occur at this point (Fig. 5*G*). Space restriction due to the Arg^{277} side chain and a different local network of hydrogen bonds presumably exclude water in the corresponding wild-type complex (Fig. 5*B*).

Proceeding with analysis of the wild-type enzyme, we find that the enol/enolate produced by decarboxylation adopts a $^2H_1$ *half-chair* conformation that is strained by the presence of the endocyclic double bond (Fig. 5*C*). We carefully examined the simulated structures for candidate groups involved in stereospecific protonation of the enolate at C_5. There are no protein residues close enough to adopt this role. However, a water molecule bonded to Glu^{120} is found in all structures in a position optimally suited for stereospecific protonation from below the sugar ring through a *Si* side attack on C_5 (Fig. 5*C*). Solvent deuterium would thus be incorporated in axial position at C_5 of UDP-xylose, in agreement with our NMR data and consistent with stereochemical analysis of the UXS reaction by Schutzbach and Feingold (16) using C_5 tritium-labeled UDP-GlcUA as substrate. The large solvent isotope effect on k_{cat} for E120A would be consistent with the proposed role for Glu^{120}. The resulting UDP-4-keto-pentose adopts a flattened $^4C_1$ *chair* (Fig. 5*D*). The reactive 4-keto group is placed suitably for stereospecific hydride transfer from NADH under general acid catalytic assistance from Tyr^{147}. The UDP-xylose product is in a relaxed $^4C_1$ conformation (data not shown), similar as in Fig. 5*D*.

The Catalytic Mechanism of hUXS1 and Its Biological Implications—A detailed proposal for the catalytic mechanism of hUXS1 is supported (Scheme 2). Having captured the relevant (stable) intermediates of the enzymatic reaction, we present here the first direct observation that conversion of UDP-GlcUA by UXS proceeds in three discrete catalytic steps. We further assign catalytic functions to the individual active site groups in each reaction step, thus revealing how the classical SDR catalytic center is expanded in UXS to accommodate the specific task of oxidative decarboxylation. Tyr^{147} is the Brøn-

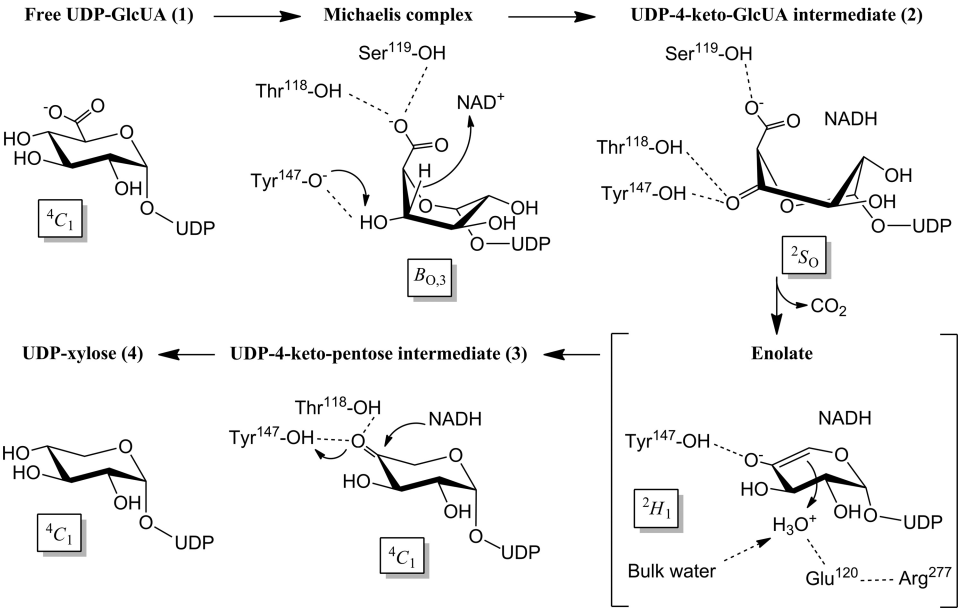

SCHEME 2. **Proposed catalytic mechanism of hUXS1.**

sted acid-base for catalytic oxidation and reduction. Mutation of the tyrosine to the incompetent phenylalanine was strongly disruptive for activity in substrate dehydrogenation and, not unexpectedly, it completely eliminated reductase activity toward the unactivated keto group in UDP-4-keto-pentose. Thr^{118} has a key role in positioning the substrate for oxidative decarboxylation by forming a strong hydrogen bond with the carboxylate group at C_5. This role differs from the canonical catalytic function of homologous threonine/serine residues in SDR active sites that is in the orientation of the reactive alcohol group on the substrate (20, 40). Arg^{277} indirectly contributes to catalysis by bonding with Glu^{120} from the neighboring loop in the structure. Thus, the binding pocket for the carboxylate group of the substrate is created, and the active site is closed up. This prevents escape of UDP-4-keto-pentose during reaction. Glu^{120} is furthermore important for stereospecific protonation of the enolate formed in the decarboxylation step. A particular component of significance of the hUXS1 mechanism is that the sugar ring pucker in the substrate/intermediates changes along the reaction coordinate to optimally underpin the chemical steps. Glu^{120} is important for the binding site to exercise strain on the enzyme-bound substrate. Destabilization of substrate is an important general mechanism of enzyme catalysis and hUXS1 appears to have found an ingenious way to apply it. Our findings furthermore provide an explanation for the interesting pattern of residue conservation in extended SDRs that Glu^{120} and Arg^{277} of hUXS1 are invariant within the UXS group of enzymes, whereas the same residues are not present in "counterpart" epimerases that prevent decarboxylation at C_5 in a highly similar transformation of UDP-GlcUA via oxidation and reduction at C_4 (11, 47) (supplemental Fig. S1). Of note, Glu^{120} and Arg^{277} of UXS are replaced, respectively, by a serine and a threonine in the epimerases. We predict that in epimerases, the pyranose ring pucker for enzyme-bound substrate and oxidized intermediate will not be the same as in UXS, thus preventing the decarboxylation. Enzymes utilizing UDP-4-keto-pentose as a key intermediate for making products other than UDP-xylose are expected to employ a mechanism of oxidative decarboxylation analogous to that of hUXS1. Molecular strategies for diversification at the level of UDP-4-keto-pentose involve "early" release of NADH as in ArnA (41–43) or catalytic pyranoside ring contraction as in UDP-α-D-apiose synthase (48, 49). The high-resolution structure of hUXS1 provides a valuable basis to further explore these alternative enzymatic reaction mechanisms. Considering the essential role of the enzyme in human extracellular matrix glycobiology, the hUXS1 structure will furthermore be of great interest for exploitation in the design of small-molecule effectors or inhibitors of the enzyme. Evidence from our MD simulations provides useful guidance to such efforts.

REFERENCES

1. Theocharis, A. D., Skandalis, S. S., Tzanakakis, G. N., and Karamanos, N. K. (2010) Proteoglycans in health and disease. Novel roles for proteoglycans in malignancy and their pharmacological targeting. *FEBS J.* **277,** 3904–3923
2. Bernfield, M., Götte, M., Park, P. W., Reizes, O., Fitzgerald, M. L., Lincecum, J., and Zako, M. (1999) Functions of cell surface heparan sulfate proteoglycans. *Annu. Rev. Biochem.* **68,** 729–777
3. Bishop, J. R., Schuksz, M., and Esko, J. D. (2007) Heparan sulfate proteoglycans fine-tune mammalian physiology. *Nature* **446,** 1030–1037
4. Iozzo, R. V. (1998) Matrix proteoglycans. From molecular design to cellular function. *Annu. Rev. Biochem.* **67,** 609–652
5. Lander, A. D., and Selleck, S. B. (2000) The elusive functions of proteoglycans. *In vivo* veritas. *J. Cell Biol.* **148,** 227–232
6. Schaefer, L., and Schaefer, R. M. (2010) Proteoglycans. From structural compounds to signaling molecules. *Cell Tissue Res.* **339,** 237–246
7. Prydz, K., and Dalen, K. T. (2000) Synthesis and sorting of proteoglycans. Commentary. *J. Cell Sci.* **113,** 193–205
8. Kearns, A. E., Vertel, B. M., and Schwartz, N. B. (1993) Topography of glycosylation and UDP-xylose production. *J. Biol. Chem.* **268,** 11097–11104
9. Moriarity, J. L., Hurt, K. J., Resnick, A. C., Storm, P. B., Laroy, W., Schnaar, R. L., and Snyder, S. H. (2002) UDP-glucuronate decarboxylase, a key enzyme in proteoglycan synthesis. Cloning, characterization, and localization. *J. Biol. Chem.* **277,** 16968–16975

10. Eames, B. F., Singer, A., Smith, G. A., Wood, Z. A., Yan, Y. L., He, X., Polizzi, S. J., Catchen, J. M., Rodriguez-Mari, A., Linbo, T., Raible, D. W., and Postlethwait, J. H. (2010) UDP xylose synthase 1 is required for morphogenesis and histogenesis of the craniofacial skeleton. *Dev. Biol.* **341,** 400–415
11. Bar-Peled, M., and O'Neill, M. A. (2011) Plant nucleotide sugar formation, interconversion, and salvage by sugar recycling. *Annu. Rev. Plant Biol.* **62,** 127–155
12. Bar-Peled, M., Griffith, C. L., and Doering, T. L. (2001) Functional cloning and characterization of a UDP-glucuronic acid decarboxylase. The pathogenic fungus *Cryptococcus neoformans* elucidates UDP-xylose synthesis. *Proc. Natl. Acad. Sci. U.S.A.* **98,** 12003–12008
13. Coyne, M. J., Fletcher, C. M., Reinap, B., and Comstock, L. E. (2011) UDP-glucuronic acid decarboxylases of *Bacteroides fragilis* and their prevalence in bacteria. *J. Bacteriol.* **193,** 5252–5259
14. Gu, X., Lee, S. G., and Bar-Peled, M. (2011) Biosynthesis of UDP-xylose and UDP-arabinose in *Sinorhizobium meliloti* 1021. First characterization of a bacterial UDP-xylose synthase, and UDP-xylose 4-epimerase. *Microbiology* **157,** 260–269
15. Rosenberger, A. F., Hangelmann, L., Hofinger, A., and Wilson, I. B. (2012) UDP-xylose and UDP-galactose synthesis in *Trichomonas vaginalis. Mol. Biochem. Parasitol.* **181,** 53–56
16. Schutzbach, J. S., and Feingold, D. S. (1970) Biosynthesis of uridine diphosphate D-xylose IV. Mechanism of action of uridine diphosphoglucuronate carboxylyase. *J. Biol. Chem.* **245,** 2476–2482
17. Gu, X., Glushka, J., Yin, Y., Xu, Y., Denny, T., Smith, J., Jiang, Y., and Bar-Peled, M. (2010) Identification of a bifunctional UDP-4-keto-pentose/UDP-xylose synthase in the plant pathogenic bacterium *Ralstonia solanacearum* strain GMI1000, a distinct member of the 4,6-dehydratase and decarboxylase family. *J. Biol. Chem.* **285,** 9030–9040
18. He, X. M., and Liu, H. W. (2002) Formation of unusual sugars. Mechanistic studies and biosynthetic applications. *Annu. Rev. Biochem.* **71,** 701–754
19. Tanner, M. E. (2008) Transient oxidation as a mechanistic strategy in enzymatic catalysis. *Curr. Opin. Chem. Biol.* **12,** 532–538
20. Kavanagh, K. L., Jörnvall, H., Persson, B., and Oppermann, U. (2008) The SDR superfamily. Functional and structural diversity within a family of metabolic and regulatory enzymes. *Cell Mol. Life Sci.* **65,** 3895–3906
21. Frey, P. A. (1996) The Leloir pathway. A mechanistic imperative for three enzymes to change the stereochemical configuration of a single carbon in galactose. *FASEB J.* **10,** 461–470
22. Thibodeaux, C. J., Melançon, C. E., and Liu, H. W. (2007) Unusual sugar biosynthesis and natural product glycodiversification. *Nature* **446,** 1008–1016
23. Collaborative Computational Project (1994) The CCP4 Suite. Programs for protein crystallography. *Acta Crystallogr. Sect. D Biol. Crystallogr.* **50,** 760–763
24. Sheldrick, G. M., and Schneider, T. R. (1997) SHELXL. High-resolution refinement. *Methods Enzymol.* **277,** 319–343
25. Emsley, P., and Cowtan, K. (2004) COOT. Model-building tools for molecular graphics. *Acta Crystallogr. Sect. D Biol. Crystallogr.* **60,** 2126–2132
26. Murshudov, G. N., Vagin, A. A., and Dodson, E. J. (1997) Refinement of macromolecular structures by the maximum-likelihood method. *Acta Crystallogr. Sect. D Biol. Crystallogr.* **53,** 240–255
27. Hess, B., Kutzner, C., van der Spoel, D., and Lindahl, E. (2008) GROMACS 4. Algorithms for highly efficient, load-balanced, and scalable molecular simulation. *J. Chem. Theory Comput.* **4,** 435–447
28. Hornak, V., Abel, R., Okur, A., Strockbine, B., Roitberg, A., and Simmerling, C. (2006) Comparison of multiple amber force fields and development of improved protein backbone parameters. *Proteins* **65,** 712–725
29. Jorgensen, W. L., Chandrasekhar, J., Madura, J. D., Impey, R. W., and Klein, M. L. (1983) Comparison of simple potential functions for simulating liquid water. *J. Chem. Phys.* **79,** 926
30. Wang, J., Wolf, R. M., Caldwell, J. W., Kollman, P. A., and Case, D. A. (2004) Development and testing of a general amber force field. *J. Comput. Chem.* **25,** 1157–1174
31. Wang, J., Wang, W., Kollman, P. A., and Case, D. A. (2006) Automatic atom-type and bond-type perception in molecular mechanical calculations. *J. Mol. Graph. Model.* **25,** 247–260
32. Mobley, D. L., Chodera, J. D., and Dill, K. A. (2006) On the use of orientational restraints and symmetry corrections in alchemical free energy calculations. *J. Chem. Phys.* **125,** 084902
33. Olsson, M. H. M., Søndergaard, C. R., Rostkowski, M., and Jensen, J. H. (2011) PROPKA3. Consistent treatment of internal and surface residues in empirical pK_a predictions. *J. Chem. Theory Comput.* **7,** 525–537
34. Hoover, W. G. (1985) Canonical dynamics. Equilibrium phase-space distributions. *Phys. Rev. A* **31,** 1695–1697
35. Essmann, U., Perera, L., Berkowitz, M. L., Darden, T., Lee, H., and Pedersen, L. G. (1995) A smooth particle mesh Ewald potential. *J. Chem. Phys.* **103,** 8577–8592
36. Berendsen, H. J. C., Postma, J. P. M., Van Gunsteren, W. F., DiNola, A., and Haak, J. R. (1984) Molecular dynamics with coupling to an external bath. *J. Chem. Phys.* **81,** 3684
37. Hess, B., Bekker, H., Berendsen, H. J., and Fraaije, J. G. (1997) LINCS. A linear constraint solver for molecular simulations. *J. Comput. Chem.* **18,** 1463–1472
38. Krezel, A., and Bal, W. (2004) A formula for correlating pK_a values determined in D_2O and H_2O. *J. Inorg. Biochem.* **98,** 161–166
39. Krissinel, E., and Henrick, K. (2007) Inference of macromolecular assemblies from crystalline state. *J. Mol. Biol.* **372,** 774–797
40. Filling, C., Berndt, K. D., Benach, J., Knapp, S., Prozorovski, T., Nordling, E., Ladenstein, R., Jörnvall, H., and Oppermann, U. (2002) Critical residues for structure and catalysis in short-chain dehydrogenases/reductases. *J. Biol. Chem.* **277,** 25677–25684
41. Gatzeva-Topalova, P. Z., May, A. P., and Sousa, M. C. (2004) Crystal structure of *Escherichia coli* ArnA (PmrI) decarboxylase domain. A key enzyme for lipid a modification with 4-amino-4-deoxy-L-arabinose and polymyxin resistance. *Biochemistry* **43,** 13370–13379
42. Gatzeva-Topalova, P. Z., May, A. P., and Sousa, M. C. (2005) Structure and mechanism of ArnA. Conformational change implies ordered dehydrogenase mechanism in key enzyme for polymyxin resistance. *Structure* **13,** 929–942
43. Williams, G. J., Breazeale, S. D., Raetz, C. R., and Naismith, J. H. (2005) Structure and function of both domains of ArnA, a dual function decarboxylase and a formyltransferase, involved in 4-amino-4-deoxy-L-arabinose biosynthesis. *J. Biol. Chem.* **280,** 23000–23008
44. Mikhailov, D., Mayo, K. H., Vlahov, I. R., Toida, T., Pervin, A., and Linhardt, R. J. (1996) NMR solution conformation of heparin-derived tetrasaccharide. *Biochem. J.* **318,** 93–102
45. Ochsenbein, P., Bonin, M., Schenk-Joss, K., and El-Hajji, M. (2011) The ^2S_O *skew-boat* conformation in L-iduronic acid. *Angew. Chem. Int. Ed.* **50,** 11637–11639
46. Pan, Y., Kee, C. W., Jiang, Z., Ma, T., Zhao, Y., Yang, Y., Xue, H., and Tan, C. H. (2011) Expanding the utility of bronsted base catalysis. Biomimetic enantioselective decarboxylative reactions. *Chem. Eur. J.* **17,** 8363–8370
47. Broach, B., Gu, X., and Bar-Peled, M. (2012) Biosynthesis of UDP-glucuronic acid and UDP-galacturonic acid in *Bacillus cereus* subsp. *cytotoxis* NVH 391–98. *FEBS J.* **279,** 100–112
48. Choi, S. H., Ruszczycky, M. W., Zhang, H., and Liu, H. W. (2011) A fluoro analogue of UDP-α-D-glucuronic acid is an inhibitor of UDP-α-D-apiose/UDP-α-D-xylose synthase. *Chem. Commun.* **47,** 10130–10132
49. Gebb, C., Baron, D., and Grisebach, H. (1975) Spectroscopic evidence for formation of a 4-keto intermediate in UDP-apiose UDP-xylose synthase reaction. *Eur. J. Biochem.* **54,** 493–498